Codoping of Sb_2Te_3 thin films with V and Cr

L. B. Duffy,[1,2] A. I. Figueroa,[3] G. van der Laan,[3] and T. Hesjedal[1,*]

[1] *Department of Physics, Clarendon Laboratory, University of Oxford, Oxford, OX1 3PU, United Kingdom*
[2] *ISIS, STFC, Rutherford Appleton Lab, Didcot, OX11 0QX, United Kingdom*
[3] *Magnetic Spectroscopy Group, Diamond Light Source, Didcot, OX11 0DE, United Kingdom*

(Dated: October 22, 2017)

Magnetically doped topological insulators (TIs) are key to realizing the quantum anomalous Hall (QAH) effect, with the prospect of enabling dissipationless electronic devices in the future. Doping of the well-established three-dimensional TIs of the $(Bi,Sb)_2(Se,Te)_3$ family with the transition metals Cr and V is now an established approach for observing the QAH state at very low temperatures. While the magnetic transition temperatures of these materials is on the order of 10's of K, full quantization of the QAH state is achieved below ∼100 mK, governed by the size of the magnetic gap and thus the out-of-plane magnetic moment. In an attempt to raise the size of the magnetic moment and transition temperature, we carried out a structural and magnetic investigation of codoped (V,Cr):Sb_2Te_3 thin films. Starting from singly doped Cr:Sb_2Te_3 films, free of secondary phases and with a transition temperature of ∼72 K, we introduced increasing fractions of V and found a doubling of the transition temperature, while the magnetic moment decreases. In order to separate the properties and contributions of the two transition metals in the complex doping scenario independently, we employed spectroscopic x-ray techniques. Surprisingly, already small amounts of V lead to the formation of the secondary phase Cr_2Te_3. No V was detectable in the Sb_2Te_3 matrix. Instead, it acts as a surfactant and can be found in the near-surface layers at the end of the growth. Our study highlights the importance of x-ray-based studies for the doping of van der Waals systems, for which the optimization of magnetic moment or transition temperature alone is not necessarily a good strategy.

PACS numbers: 75.30.Hx; 78.70.Dm; 75.50.Pp; 73.61.Ng

I. INTRODUCTION

The pursuit of low power-consumption electronic devices has lead to intense interest in topologically nontrivial electronic band structure materials such as topological insulators (TIs) [1]. Their bulk is gapped, however, strong spin-orbit coupling leads to gapless conducting surface states which are time reversal symmetry (TRS) protected. This makes these topological surface states (TSSs) immune to both non-magnetic impurities and geometric perturbations. Magnetic topological insulators (MTIs) [2–5], in which TRS is broken, show a finite gap in the Dirac cone of the TSSs — a prerequisite for the observation of the quantum anomalous Hall (QAH) effect [5]. The QAH effect is key for future electronic devices, as its precisely quantized dissipationless transport does not require the application of a magnetic field.

It has previously been demonstrated that MTIs can be realized by magnetically doping three-dimensional TI materials of the $(Bi,Sb)_2(Se,Te)_3$ type with transition metals such as Mn [6–8] and Fe [9], and more recently Cr and V [10–14]. In both V- and Cr-doped $(Bi,Sb)_2Te_3$ epitaxial thin films, the QAH effect has been successfully demonstrated [4, 13, 15, 16] at extremely low temperatures (<100 mK). Doping Sb_2Te_3 with V has been reported to exhibit a more stable long-range ferromagnetic order than that of Cr-doped films [17], while retaining high magnetic transition temperatures [18, 19]. The mechanism behind the induced long-range ferromagnetic order within these materials, however, is still not completely understood [3, 12, 17, 20–26]. Members of this family of materials are layered compounds with a hexagonal crystal structure, and electrically narrow-gap semiconductors with an indirect band gap (e.g., ∼160 meV for Bi_2Te_3). Their unit cell is characterized by three Se/Te-Bi/Sb-Se/Te-Bi/Sb-Se/Te quintuple layers, which are weakly bonded via the van der Waals gap. Owing to the layered crystal structure, the controlled, substitutional doping of these materials has been proven difficult. In fact, from earlier work on electric contacts in the context of thermoelectric applications [27], it has been known that metals in contact with these materials deteriorate. Diffusion and reaction of the metals occur already at moderate temperatures, and in some cases even down to room temperature [28]. The resulting inhomogeneities will affect the structural and magnetic properties [26, 29], and will result in inconsistencies in the reported literature in terms of carrier concentrations, magnetic transition temperatures, saturation magnetizations, and magnetic anisotropies. For instance, in case of Mn-doped Bi_2Te_3, extended x-ray absorption fine structure spectroscopy in combination with electron energy loss spectroscopy revealed that Mn is substitutionally doping on Bi and Te sites, but can also reside in the van der Waals gap [30]. Consequently, ferromagnetism in this material (e.g., T_c≈10 K in 10% doped thin films [31]) can be due to homogeneous doping, either on Bi or Te sites, interlayer positions in the van der Waals gap, or secondary

* Thorsten.Hesjedal@physics.ox.ac.uk

Mn-containing phases.

Owing to the success of Cr and V doping of Sb_2Te_3 in terms of demonstrating the QAH effect, it is interesting to explore codoping in an attempt to make use of the respective superior properties to optimize the magnetic gap, which is proportional to the out-of-plane magnetic moment. This codoping strategy is well-established for obtaining high-performance permanent magnets in which high-moment rare earth elements are alloyed with high-coercivity transition metals. In case of MTIs, it is of interest to combine the higher magnetic moment of Cr with the larger coercivity of V dopants. In dilute magnetic semiconductors, codoping is further predicted to lead to enhanced magnetic properties due to the interplay between the spin-polarized magnetic defects [32]. In fact, V-Cr codoping of Sb_2Te_3 bulk crystals has been reported by Uher's group already in 2007 [33], and they observed an increased remanent magnetization for $Sb_{1.98-x}V_{0.02}Cr_xTe_3$ ($0< x <0.022$), while the transition temperatures were with ∼20 K comparable to only Cr-doped crystals. On the other hand, understanding and controlling the complex defect chemistry and formation of secondary phases is a great challenge in quaternary materials, in particular in thin films where grain boundaries are present. Fortunately, it has been shown that the resultant magnetic disorder, i.e., strongly pinned domains, are not affecting the precisely quantized QAH effect [34].

It is therefore of utmost importance to study the doping scenario in great detail — both in terms of structural and chemical properties, which ultimately determine the electronic and magnetic properties. The combination of synchrotron-based spectroscopies in the soft and hard x-ray range have been used to determine the structural, chemical, and magnetic properties in a reliable way for dilute magnetic semiconductors and TIs alike [11, 35, 36]. While x-ray absorption fine structure (XAFS) measurements and analysis provide access to the position of the dopants in an element-specific way, soft x-ray absorption and magnetic dichroism reveal the oxidation state and magnetic properties of the transition metal dopants. X-ray magnetic circular dichroism (XMCD) is further capable of probing with varying surface sensitivity, through the simultaneous recording of total electron-yield (TEY) and fluorescence yield (FY) signals, the individual contributions of dopants in a codoping scenario — a piece of information not accessible in conventional magnetometry. Due to the difference in probing depth, the TEY probes mainly the top ∼5 nm at the surface while the FY probes the bulk of the thin film [35]. XMCD has been intensely used to probe the local electronic structure of the magnetic ground state of mono-doped MTIs [11, 29, 37–40].

Here, we use x-ray absorption spectroscopy (XAS), XAFS measurements and analysis, and XMCD to investigate in detail the structural and magnetic properties of V and Cr codoped Sb_2Te_3. Compared to the more common method of doping TIs with just one transition-metal or rare-earth element, codoping is a rarely employed approach for encouraging the formation of long-range ferromagnetic order at temperatures far more accessible for device applications, e.g., by combining high transition temperature with large magnetic moment elements. Codoping a $3d$- or $4f$-doped material, with another $3d$ or $4f$ dopant, has been shown using density functional theory to potentially lead to stable long-range ferromagnetic order, combining large magnetic moments with low levels of defects [41]. It has also been predicted that this approach could also allow for tuning of the Fermi level of the TI by varying the doping concentrations such that it resides in the gap of the opened TSS [41].

II. EXPERIMENTAL METHODS

A. Thin film growth, structural and magnetic characterization

The codoped Sb_2Te_3 thin film samples were grown on c-plane sapphire substrates via codeposition in a molecular beam epitaxy (MBE) system with a base pressure of 1×10^{-10} mbar. Before baking in UHV, the substrates were solvent-cleaned and rinsed in DI water. Te and Sb (6N purity) were evaporated out of standard effusion cells, and Cr and V (4N purity) out of high-temperature cells. A Te:Sb flux ratio of 10:1 was maintained throughout the growth of all samples, as measured by an *in-situ* beam flux monitor (BFM), to reduce the density of Te vacancies. We employed a two-step deposition method [10, 42], whereby first a ∼5-nm-thick undoped Sb_2Te_3 layer was grown at a lower substrate temperature of 200°C, and then annealed at 250°C while supplying Te. The subsequent growth of the codoped (V,Cr):Sb_2Te_3 layers was performed at 250°C. The Cr flux was kept the same for all films. For the case of pure Cr-doping, where Cr is substitutional on the Sb sites [10], i.e., $Cr_xSb_{1-x}Te_3$, x was determined to be ∼0.06. The V flux was varied between 10% and 40% of the Cr flux. Unless otherwise noted, the measurements were carried out on a sample with a nominal V:Cr flux ratio of 1:5.

In-situ reflection high energy electron diffraction (RHEED) was used to observe the surface morphology of the thin films during growth. The films exhibit a streaky RHEED pattern, indicative of smooth 2D growth (cf. Ref. [10]). By performing azimuthal rotations, it was observed that the samples have three-fold symmetry, consistent with the space group $R\bar{3}m$.

X-ray reflectometry (XRR) and x-ray diffraction (XRD) were carried out on a Bruker D8 diffractometer using Cu $K\alpha_1$ radiation, to obtain the film thickness and roughness, as well as to determine the crystalline phases and crystal quality of the films, respectively.

Magnetization measurements were carried out in a SQUID magnetometer (Quantum Design MPMS). The samples were mounted with the field applied in-plane ($\perp$ c-axis) or out-of-plane ($\parallel$ c-axis), respectively.

B. XAS and XMCD

X-ray absorption spectroscopy (XAS) was performed in the 14-T-magnet on beamline I10 (BLADE) at the Diamond Light Source (Didcot, UK), which provides a UHV sample environment with a base temperature of ∼2.5 K. Measurements were performed at the $L_{2,3}$ edges of Cr (570-590 eV) and V (500-525 eV), and the $M_{4,5}$ edges of Sb (525-545 eV), on codoped and Cr-doped Sb_2Te_3 thin films. The XMCD is obtained by subtracting XAS spectra measured with the x-ray helicity vector anti-parallel and parallel to the applied magnetic field. For the TEY measurements, the drain current was measured from the electrically grounded samples. The FY signal was obtained using a photodiode placed near the sample surface. Measurements were taken both in normal (∥ c-axis) and grazing (30° off c-axis) incidence, whereby the magnetic field was applied along the x-ray beam (∼20×100 μm^2 spot size). In order to obtain a pristine surface, the samples were cleaved for the soft x-ray studies in the magnet in ultrahigh vacuum, resulting in metal-like elemental spectra. For cleaving the films, a post was glued onto the samples and knocked-off in the magnet prior to the measurements, essentially removing the top surface of the film. Owing to the layered crystal structure with a van der Waals gap, the films cleave quite readily.

C. X-ray absorption fine structure (XAFS) measurements and analysis

X-ray absorption near edge structure (XANES) and extended x-ray absorption fine structure (EXAFS) were measured at the V and Cr K-edges (∼5465 and ∼5989 eV, respectively) at room temperature on beamline B18 at the Diamond Light Source on uncleaved samples. A nine-element solid-state Ge detector with digital signal processing for fluorescence detection, high energy resolution, and high count rate was used to measure with the beam at 45° incidence with respect to the sample plane. All spectra were acquired in quick-EXAFS mode, using the Pt-coated branch of collimating and focusing mirrors, a Si(111) double-crystal monochromator and a pair of harmonic rejection mirrors. The energy range for each scan at the Cr K-edge allowed us to extract information in the extended region up to $k = 14$ Å^{-1}. V and Cr foils of 5 μm thickness were measured as references.

The EXAFS spectra were processed and analyzed using different tools of the IFFEFIT XAFS package [43]. This involved preliminary reduction of the EXAFS raw data, background removal of the x-ray absorption data $\mu(E)$, conversion of $\mu(E)$ to $\chi(k)$, normalization and weighting scheme; all of them performed with AUTOBK and ATHENA. EXAFS data analysis and fits were performed in ARTEMIS, making use of models based on crystallographic information obtained from the ICSD database. The atomic clusters used to get the scattering paths for fitting were generated with ATOMS [44].

III. RESULTS

A. Temperature dependence of the magnetic properties

SQUID measurements of magnetization as a function of temperature and applied field, as shown in Fig. 1, were performed on the samples in order to observe their bulk transition temperatures. The Cr-doped Sb_2Te_3 sample (with the same Cr concentration) showed a $T_c = 72$ K, while the T_c of the codoped samples was also a function of the V concentration. The highest T_c of 148 K was reached for the codoped sample with a V:Cr ratio of 1:5, while the T_c was lower for both lower and higher V concentrations, reaching down to 5 K at both ends of the concentration range. However, the Cr:Sb_2Te_3 sample appears to have a higher magnetic moment than the optimally doped (V,Cr):Sb_2Te_3 sample, and a lower saturation field. To study the origin of the underlying doping behavior, we have carried out magnetic spectroscopy of the codoped sample with the highest transition temperature.

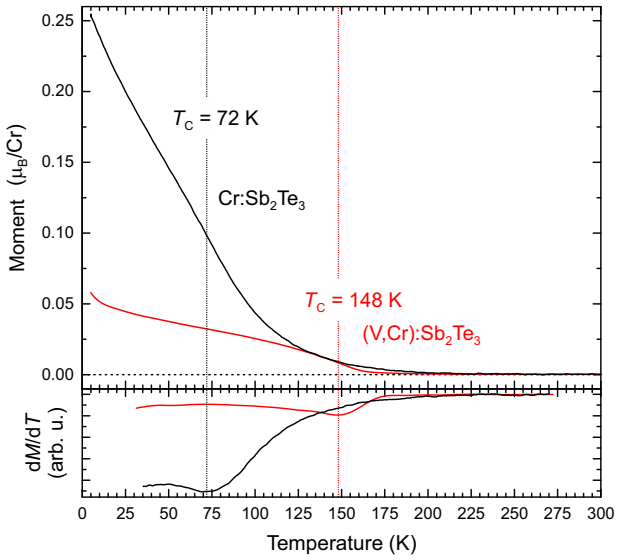

FIG. 1. Magnetization as a function of temperature, $M(T)$, for both the Cr-doped and codoped sample measured whilst cooling in a 20 mT applied in-plane field. Note that the calculated moment per Cr ion assumes substitutional doping on Sb sites. The transition temperature, T_c, is defined within the Landau theory of phase transitions as the minimum of the derivative as shown in the lower panel [45].

XAS and XMCD measurements were performed after cleaving the thin film samples in the UHV spectroscopy chamber to ensure a pristine surface. The temperature-dependent XMCD plots shown in Fig. 2 were measured in TEY mode on the $L_{2,3}$ edge of Cr. Note that the V

XAS signal at the $L_{2,3}$ edge was too noisy to obtain an XMCD signal. By comparing the element-specific transition temperature for Cr, defined as the temperature at which the XMCD signal completely vanishes, with the SQUID results in Fig. 1, which average over all magnetic contributions, it is in principle possible to disentangle the individual contributions of both magnetic species. From this comparison, it is clear that for both samples Cr is mainly responsible for the magnetic bulk properties of the sample. This suggests that for the codoped sample, V does not seem to contribute significantly to the ferromagnetic order directly. Note that we have therefore given the magnetic moment of the sample in Fig. 1 as a moment per Cr ion, assuming substitutional Cr doping on Sb sites, as previously confirmed for purely Cr-doped Sb_2Te_3 [10]. In this doping scenario, however, it is not clear why the Cr moment is reduced by a factor of ∼5 in the codoped samples.

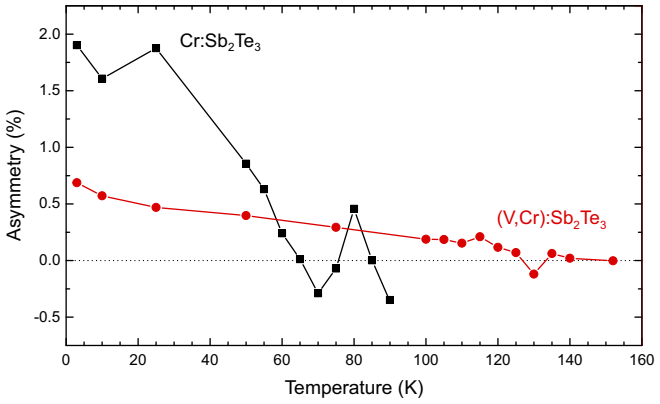

FIG. 2. XMCD asymmetry (TEY) measured at the Cr L_3 edge in zero field (after saturating the sample in a field of 8 T) at 30° grazing incidence for both the Cr-doped and codoped sample as a function of temperature. The magnetic behavior of the Cr in both samples follows closely the SQUID data, shown in Fig. 1, demonstrating that the magnetic properties of both samples can be attributed to Cr. For the codoped sample this indicates that V does not appear to have a significant magnetic contribution.

Figure 3 shows the XMCD and SQUID hysteresis plots for both samples with the field applied in-plane. The diamagnetic contribution of the Al_2O_3 substrate has been subtracted in the SQUID data by using a linear fit to the high-field region of the magnetization curve. The XMCD hysteresis loop plots the intensity change of the Cr L_3 peak.

The codoped sample [Fig. 3(a)] shows a saturation field of ∼5 T in the SQUID data, whereas the XMCD data do not seem to saturate even at the highest applied field of 7 T, however, the increase with field is slow beyond 5 T. The magnetic moment in the SQUID data has been scaled to show the magnetic moment per Cr ion, taking into account the volume of the sample as calculated from the thickness of the film [XRR data; see Fig. 4(b)] and the sample area. As discussed earlier, the XMCD measurements as a function of temperature confirm that V does not contribute significantly to the magnetic properties of the material, therefore it is sensible to only take into account the Cr concentration. The saturation magnetization of the codoped sample is (0.35 ± 0.2) μ_B/Cr with the uncertainty dominated by the determination of the film volume. Note that the difference of moments at 5 K compared to Fig. 1 is due to the different applied field values. The XMCD data is slightly offset in comparison to the SQUID magnetometer data as the sample was measured at 30° grazing incidence. The XMCD data shows that the hysteresis loop closes at ∼1.5 T.

The Cr:Sb_2Te_3 sample [Fig. 3(b)] is in comparison saturated by an in-plane applied field between 1 and 1.5 T, consistent with previously published data [10]. The saturation moment of (3 ± 0.2) μ_B/Cr ion is also in agreement with previously published data, with the error once again dominated by the determination of film volume.

This demonstrates that, despite the promising increase in T_c by codoping, the saturation moment due to the addition of V is much lower. As we will see in the next section, the occurrence of the Cr_2Te_3 phase could be held responsible for this decrease. Cr_2Te_3, as well as many of the other Cr-Te compounds, is ferromagnetic with a stoichiometry-dependent transition temperature between 180 and 340 K [46]. The magnetic moment in epitaxial thin film Cr_2Te_3, however, is with 2.8 μ_B/Cr very close to the free ion moment of 3 μ_B/Cr [46] — and not an order of magnitude smaller. On the other hand, the whole $Cr_{1-\delta}Te$ series (Cr_2Te_3 has a δ of 0.33) is known to exhibit complex magnetic coupling scenarios [47], in which the Cr on different lattice sites can couple not only ferromagnetically, but also antiferromagnetically, leading to a reduced moment [48]. Moreover, a Cr-Te phase could further magnetically couple to the Cr:Sb_2Te_3 matrix, at least below its transition temperature of 72 K, and further modify the magnetic film behavior. Finally, the reduced moment seen in the codoped film could simply be due to the fact that the effective Cr density in the unit cell is not properly taken into account. To clarify this point, a closer look at the structural and chemical properties was taken using EXAFS, XAS and XMCD.

B. Structural characterization by XRD and x-ray spectroscopy

Figure 4(a) presents XRD data for the investigated films. The Al_2O_3 (0001) substrate and (undoped) Sb_2Te_3 film peak positions have been labeled (ICSD 2084). It is clear that the Cr:Sb_2Te_3 sample is well-ordered with the c-axis parallel to the surface normal. The expected reduction in c-axis lattice parameter upon Cr doping is demonstrated by a shift of the peak positions to higher angles when compared to an undoped Sb_2Te_3 sample, consistent with Sb being substituted by Cr. The codoped (V,Cr):Sb_2Te_3 sample does not show this same reduc-

tion and demonstrates the presence of the Cr_2Te_3 phase (ICSD 15038). On the other hand, there does not appear to be any V-Te compound present, such as VTe (ICSD 52509) or V_3Te_4 (ICSD 52510), nor any metallic V, as none of the lines (shown for polycrystalline material) match any of the peaks in the experimental spectrum.

XRR data for both samples is shown in Fig. 4(b). For both samples, thickness fringes are clearly visible indicating that the interfaces are of a high quality. The periodicity of the fringes can be used to determine the thickness of each sample. The Cr:Sb_2Te_3 sample has a thickness of 60 nm and the (V,Cr):Sb_2Te_3 has a thickness of 30 nm.

XAS measurements at Cr $L_{2,3}$ edges for both the (V,Cr):Sb_2Te_3 and Cr:Sb_2Te_3 samples (see Fig. 5) show that the Cr for the codoped sample has a different lineshape to that of the Cr-doped sample, further supporting the previous conclusion that Cr is incorporated differently in these samples. It is also interesting to note that

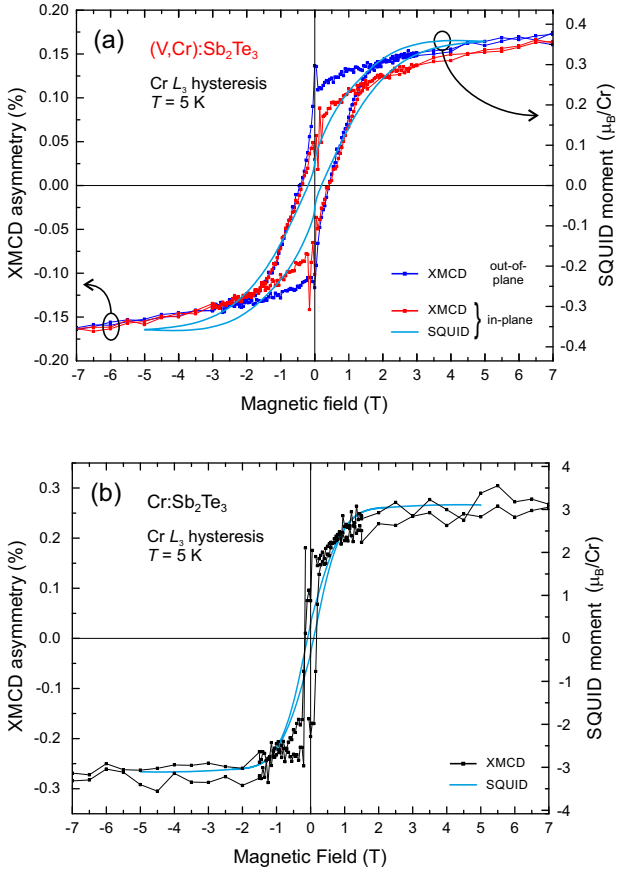

FIG. 3. Magnetization as a function of field, $M(H)$, at 5 K for (a) the codoped and (b) the Cr-doped sample. The plots compare the SQUID hysteresis with the XMCD asymmetry (TEY) at the Cr L_3 edge with the field applied in-plane. In (a), the XMCD asymmetry is also shown for the field applied out-of-plane for the codoped sample (blue curve), revealing a weak out-of-plane anisotropy.

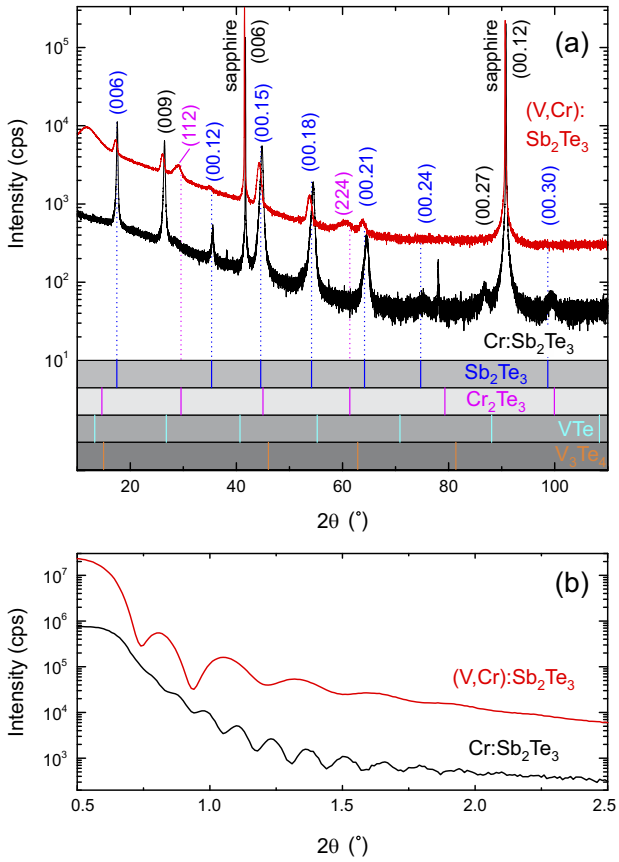

FIG. 4. (a) XRD for Cr-doped and (V,Cr)-doped Sb_2Te_3 films. The Sb_2Te_3 (blue) and Cr_2Te_3 (pink) peak positions have been labeled. Below, the barcode indicates the positions of the lines belonging to possible V-Te compounds. Note that the unlabeled peaks in case of the Cr-doped sample are due to the Al sample holder. (b) XRR data for the same samples indicating thickness fringes which occur for high quality thin films.

the Cr XMCD signal is opposite to that of the Sb in the Cr-doped sample, which is to be expected for a superexchange interaction within magnetically doped TIs [17]. As demonstrated by the SQUID measurements, the XMCD signal from the Cr is weaker for the codoped sample compared to the Cr-doped sample.

When observing the XMCD signal at the Sb $M_{4,5}$ edges of the (V,Cr):Sb_2Te_3, it is clear that Sb shows no magnetic ordering in an applied field of 8 T [see Fig. 6]. Also, the Cr:Sb_2Te_3 sample does show an XMCD signal, which is due to Sb mediating the long range ferromagnetic order within the magnetically doped TI through a superexchange interaction with the magnetic ions which substitutionally replace Sb [17, 49]. This suggests that V and Cr are not replacing Sb substitutionally in the codoped samples, disabling the superexchange mechanism via Sb.

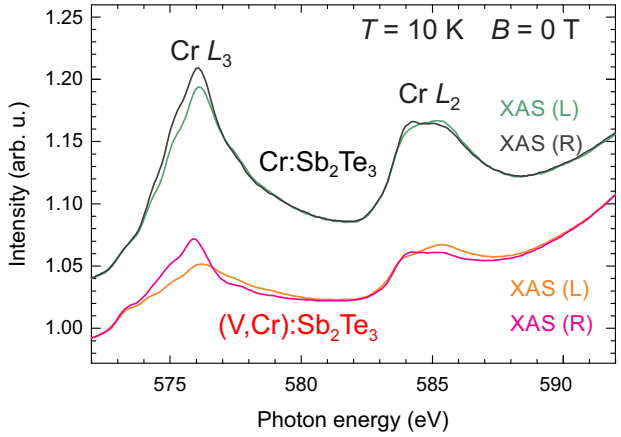

FIG. 5. Cr $L_{2,3}$ XAS of *in-situ* cleaved codoped and Cr-doped films, measured at 10 K in zero field with x-rays under normal incidence (TEY signal).

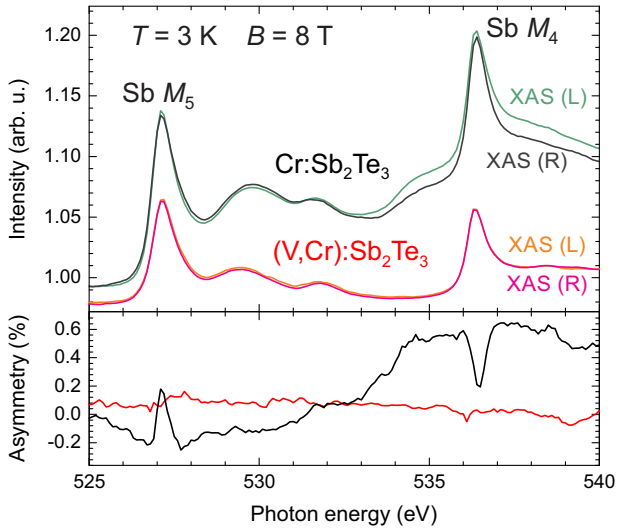

FIG. 6. XAS and XMCD measurements (TEY) for the codoped and Cr-doped film measured at the Sb $M_{4,5}$ edges ($3d \rightarrow 5p$) in 8 T field at 3 K. (a) XAS measured using left (L)-circularly (light gray and orange curves) and right (R)-circularly (dark gray and magenta curves) polarized x-rays. (b) Corresponding XMCD. The XMCD signals demonstrate that the Sb atoms within the Cr-doped samples show a magnetic moment, whereas the Sb atoms in the codoped sample do not.

C. Advanced structural characterization by XANES and EXAFS

Normalized XANES of the (V,Cr):Sb_2Te_3 film at the V K edge is plotted in Fig. 7 together with the spectrum for a V foil. The signal of this sample is very weak due to the low content of V. Comparison with the spectrum of the foil suggests that V is in its metallic form. Unfortunately, an EXAFS analysis at the V K edge is not possible due poor statistics.

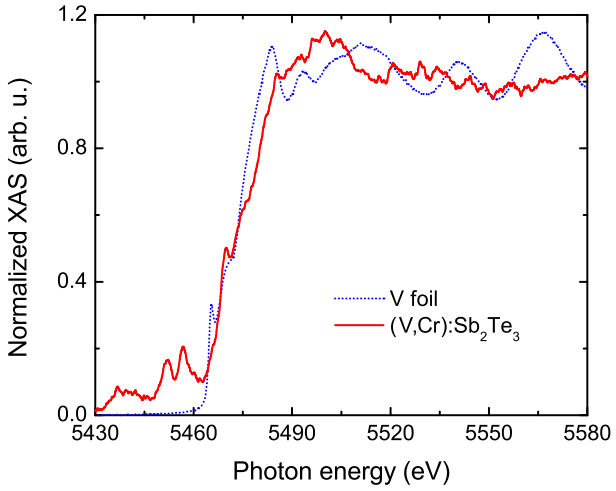

FIG. 7. Normalized V K-edge XANES spectrum of the (V,Cr):Sb_2Te_3 film together with that of a V foil for comparison.

XANES at the Cr K edge is depicted in Fig. 8(a) where the spectrum for the (V,Cr):Sb_2Te_3 film is compared to that of a Cr:Sb_2Te_3 film, CrSe and Cr foil. XANES spectra of both films are very different, revealing a different electronic environment for the Cr atoms in each case. The spectral lineshape for the (V,Cr):Sb_2Te_3 film is very similar to that observed for the Cr_2Te_3 compound in Ref. 50. However, the energy position of the edge jump in both (V,Cr):Sb_2Te_3 and Cr:Sb_2Te_3 films is the same as for the reference sample CrSe, suggesting a similar local electronic state, in which the Cr is mainly divalent.

Fits of the Cr K-edge EXAFS signal were performed in order to extract information about bond distances and coordination of the Cr atoms in both (V,Cr):Sb_2Te_3 and Cr:Sb_2Te_3 films. Figures 8(b,c) show the raw $\chi(k)$ EXAFS signal and module of the Fourier transform (FT), respectively, performed over a [2.5-12] Å^{-1} k-range using a Kaiser-Bessel window function, and $\Delta k = 2$ Å^{-1}. Plots are performed using a k^2 weight. Fits were performed on the R-space in a [1.7-3] Å range using a Kaiser-Bessel window function, so that it covered the first coordination shell. The parameters fitted were the interatomic distance (R), the Debye-Waller factor (σ^2) for each scattering path and the threshold energy (ΔE_0). The coordination number N for the (V,Cr):Sb_2Te_3 sample was also fitted. The amplitude reduction factor S_0^2 was set to that obtained for the fit of the Cr foil ($S_0^2 = 0.7$). Results of the fits are listed in Table I.

Analysis of the EXAFS results show that the first coordination shell is composed of Te atoms, with Cr-Te distances around 2.76 and 2.71 Å for the Cr:Sb_2Te_3 and (V,Cr):Sb_2Te_3 films, respectively. For the former, this R value together with a coordination number of $N = 6$ is consistent with Cr entering substitutionally into the Sb

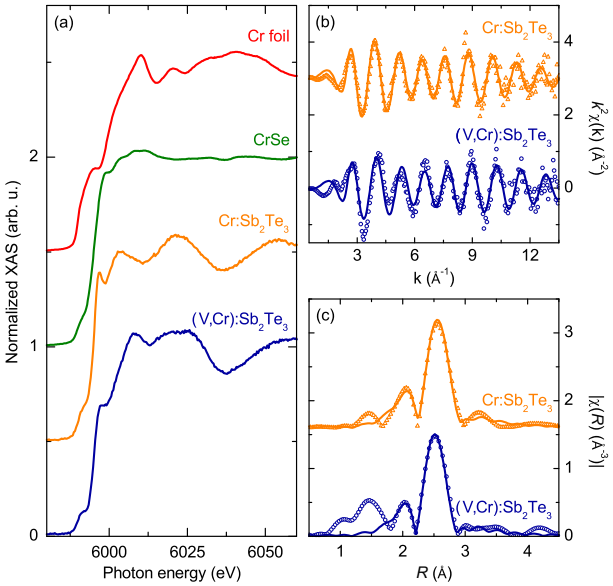

FIG. 8. X-ray absorption spectra of the (V,Cr):Sb_2Te_3 film at the Cr K edge. (a) XANES spectrum and comparison with relevant references: Cr:Sb_2Te_3 film, CrSe in powder form, and Cr foil. (b) EXAFS signals (symbols) of the films together with their best fit (solid lines). (c) Fourier transform of the EXAFS signals in (b) (symbols) together with the best fit to the first coordination shell (solid line). Spectra have been vertically shifted for clarity.

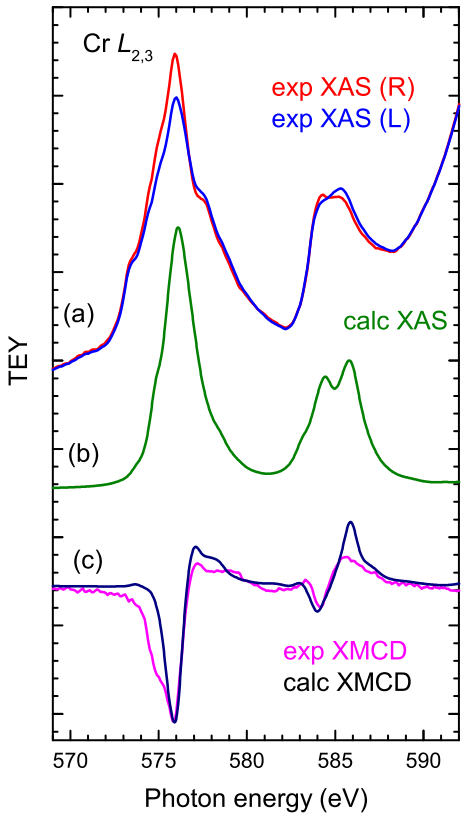

FIG. 9. Cr $L_{2,3}$ XAS and XMCD of the *in-situ* cleaved (V,Cr):Sb_2Te_3 film measured with TEY in 5 T field at 3 K at 30° grazing incidence of the x-rays. (a) Experimental spectra for left (L)- and right (R)- circularly polarized x-rays. (b) Calculated average XAS. (c) The corresponding experimental and calculated XMCD spectra.

TABLE I. Structural parameters obtained from Cr K-edge EXAFS fits for the Cr:Sb_2Te_3 and (V,Cr):Sb_2Te_3 films. Coordination number, N, interatomic distance, R, and Debye-Waller factor, σ^2, for each path. Numbers in brackets correspond to the uncertainty referred to the last digit of each value listed.

Sample	N_{Te}	$R_{\mathrm{Cr-Te}}$ (Å)	σ^2 (Å^2)	ΔE_0 (eV)
Cr:Sb_2Te_3	6	2.76(1)	0.008(2)	-1.13(6)
(V,Cr):Sb_2Te_3	4.5(2)	2.71(1)	0.006(2)	-0.56(6)

sites with octahedral symmetry. For the (V,Cr):Sb_2Te_3 film, a shorter Cr-Te distance suggests the presence of Cr_2Te_3 in the sample, which has a $R_{\mathrm{Cr-Te}} = 2.706$ Å according to the crystallographic information (ICSD 15038). The lower coordination number of $N = 4.5$ is further indicative of cluster formation.

D. XMCD Multiplet calculations

Atomic multiplet theory is used to calculate the electric-dipole transitions $3d^n \rightarrow 2p^5 3d^{n+1}$, where the spin-orbit and electrostatic interactions are treated on an equal footing [51, 52]. The wave functions of the initial- and final-state configurations are calculated in intermediate coupling using Cowan's atomic Hartree-Fock (HF) code with relativistic corrections [53, 54]. The atomic electrostatic interactions include the $2p$-$3d$ and $3d$-$3d$ Coulomb and exchange interactions, which are reduced to 70% of their atomic HF value to account for the intra-atomic screening [51]. Hybridization effects are included by mixing $3d^n$ with $3d^{n+1}\underline{L}$ configurations with a transfer integral V, where $\underline{L}$ represents an electron state of appropriate symmetry on the neighboring atoms.

X-ray spectroscopy can be used to determine the valence state of the Cr dopants, thus allowing for a determination of their environment [35]. The local ground state of Cr in Cr_2Te_3 is taken as a mixture of $\psi(d^3)$ and $\psi(d^4\underline{L})$ with a transfer integral V between these two states. Similar to Yaji *et al.* [55] we use a mixed ground state of 54% Cr^{3+} d^3 and 46% Cr^{2+} $d^4\underline{L}$ with parameters $\Delta_i \equiv E(3d^4\underline{L}) - E(3d^3) = 0$ eV and, because in the presence of a core hole the $3d$ electrons are pulled down in energy, $\Delta_f \equiv E(2p^5 3d^4\underline{L}) - E(2p^5 3d^3) = -1$ eV, an octahedral crystal field of $10Dq = 1.5$ eV, and a mixing $V = 1.5$ eV. The calculated Cr L_3 (L_2) line spectra are broadened by a Lorentzian with a half-width at half-maximum of $\Gamma = 0.3$ eV (0.4 eV) for intrinsic lifetime broadening

and a Gaussian with a standard deviation of $\sigma = 0.15$ eV for the instrumental broadening. Figures 9(b,c) show the calculated XAS and XMCD, respectively. The comparison with the experimental spectra of (V,Cr):Sb_2Te_3 [Fig. 9(a)] suggests that the dominant contribution can be due to Cr_2Te_3, but that other contributions are also present.

The covalent character of Cr_2Te_3 can be ascribed to the hybridization between the Cr $d(e_g)$ and the Te p bands, which are located just above and below the Fermi level, respectively.

The results for the covalent compound Cr_2Te_3 (54% d^3 and 46% d^4) differ from that of $Cr_xSb_{2-x}Te_3$ (Ref. 17) and $Cr_xBi_{2-x}Se_3$ (Refs. 11 and 56), where the Cr substitutionally replaces Sb and Bi, respectively. In this case, the Cr is nominally divalent (30% d^3 and 70% d^4).

IV. DISCUSSION

Our study highlights the difficulties of doping thin films of the $(Bi,Sb)_2(Se,Te)_3$ family of compounds, which is characterized by its layered crystal structure. Doping with a single element, such as Cr [10, 57] or V [12, 16, 19, 25], results in ferromagnetically ordered films with a sizable T_c and decent crystalline properties, i.e., without the occurrence of secondary phases up to rather high doping concentrations. On the other hand, adding very small amounts of another dopant, in our case V added to Cr:Sb_2Te_3, seems to force the formation of the direct telluride Cr_2Te_3 and prevent the substitutional incorporation of the dopants.

There are two possible doping scenarios that could explain this finding: (i) *Preferential V incorporation.* If V is preferential incorporated as a dopant on Sb sites, Cr could be forced out into the van der Waals gap. As we know from XAS that there is no metallic Cr present (e.g., in the form of clusters), it could instead form Cr_2Te_3 in this space between the Te layers. In this scenario, however, we would expect to find the magnetic properties of the film still being dominated by Cr:Sb_2Te_3 as only 20% of the Cr dopants are replaced by V. Also, in SQUID magnetometry, one should expect two transition temperatures corresponding to Cr:Sb_2Te_3 (∼70 K for the particular Cr concentration) and Cr_2Te_3 (∼170 K bulk value [58, 59]). Further, the out-of-plane lattice constant should increase, and the film diffraction peak should broaden significantly due to the disordered formation of Cr_2Te_3 in the gap. In summary, there is no experimental evidence for this scenario. (ii) *Surfactant-driven scenario.* If V acts as a surfactant during film growth, i.e., no (or only a small amount) of the material is incorporated, the growth mode could still be severely altered. In a surfactant-assisted growth scenario, one would expect to find the surfactant segregated on the surface after terminating the growth. Indeed, XAS at the V $L_{2,3}$ edges [cf. Fig. 10] reveals a large concentration of V on the surface of the uncleaved wafer. As a result of the *ex vacuo* transfer, the V is oxidized. The lineshape of the as-grown sample strongly resembles that of V^{5+} [60, 61], which corresponds to a stable oxidation state [62]. Contrary to the TEY, the FY shows no V peaks, which means that this element is mainly found at the surface and not in the bulk. After cleaving the sample *in situ*, only a very small amount of V is detectable at a lower-lying layer of the film. The peaks are shifted to lower photon energy, meaning a lower oxidation state for the V atoms [63]. The lineshape of the cleaved sample is consistent with the XAS spectra previously reported for V:$(Bi,Sb)_2Te_3$ [12, 24, 25].

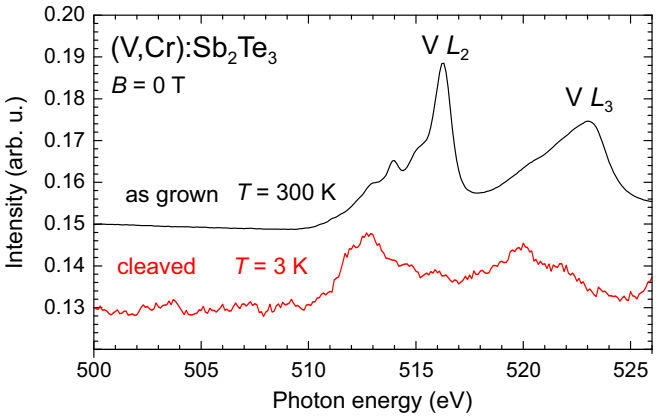

FIG. 10. XAS of the (V,Cr):Sb_2Te_3 film at the V $L_{2,3}$ edges in a field of 0 T at 30° grazing incidence of the incoming x-rays (in TEY mode). The uncleaved (as grown) sample shows a large V signal (black line), corresponding to oxidized V (after transport through air) at or near the surface of the film. After cleaving, a lower-lying layer of the sample is measured, which does not suffer from oxidation. Nevertheless, the V signal (red line) is very weak and noisy, even at 3 K, which increases the XAS signal in general. (Note that the uncleaved sample has been measured at 300 K). This finding supports a surfactant-assisted growth mode, in which V floats on the surface of the growing film, and is removed after cleaving.

We can therefore conclude that V acts as a segregating species, a surfactant, that promotes the formation of Cr_2Te_3. The opposite constellation, i.e., Cr preventing the incorporation of V and the formation of a V-Te compound, was not observed. Whereas Cr is able to form hexagonal Cr_2Te_3, which is crystallographically 'compatible' with the Sb_2Te_3 matrix, the V-Te binary phase diagram would only allow for V_3Te_4 to form, which is a monoclinic system. Surfactants have a long history in thin film growth, starting with As as a surfactant to improve the quality of Si-Ge interfaces [64]. In general, the function of the surfactant is to alter the adatom kinetics, often with the goal to promote layer-by-layer growth [65, 66]. In the layered $(Bi,Sb)_2(Se,Te)_3$-type MTIs, the surfactant seems to improve the Sb_2Te_3 host materials' crystalline quality by expelling the desired dopant (here Cr) from the matrix [67].

V. SUMMARY AND CONCLUSIONS

It is apparent from these results that magnetic doping of a TI with more than one dopant, a method explored in an attempt to enhance the magnetic moment and transition temperature, is not promising in the case of the combination of Cr and V. Using XAS, XMCD, and EXAFS in combination with standard structural and magnetic characterization techniques, we have demonstrated that V has the undesired effect of preventing Cr from substitutionally doping into the TI on Sb sites. Instead it causes the system to form Cr_2Te_3 within the sample, consistent with the much enhanced transition temperature of the codoped sample. V, on the other hand, does not contribute significantly to the magnetic properties of the sample. Note that the effects of this rather undesired doping scenario on the electronic transport properties at very low temperatures may not be affected in a detrimental way, and the observation of the precisely quantized QAH effect may still be possible [34]. Nevertheless, this experiment has demonstrated the importance of XMCD for exploring the origins of magnetic ordering in MTIs.

VI. ACKNOWLEDGMENTS

This work arises from research funded by the John Fell Oxford University Press Research Fund. We acknowledge XMCD beamtime on I10 at the Diamond Light Source (DLS) under proposal SI-13759 as well as XANES and EXAFS beamtime on B18 at DLS under proposal SP-15702. LBD acknowledges financial support from EPSRC and the Science and Technology Facilities Council (UK).

[1] L. Fu, C. L. Kane, and E. J. Mele, Phys. Rev. Lett. **98**, 106803 (2007).
[2] M. Z. Hasan and C. L. Kane, Rev. Mod. Phys. **82**, 3045 (2010).
[3] R. Yu, W. Zhang, H.-J. Zhang, S.-C. Zhang, X. Dai, and Z. Fang, Science **329**, 61 (2010).
[4] Y. Jiang, C. Song, Z. Li, M. Chen, R. L. Greene, K. He, L. Wang, X. Chen, X. Ma, and Q.-K. Xue, Phys. Rev. B **92**, 195418 (2015).
[5] H. Weng, R. Yu, X. Hu, X. Dai, and Z. Fang, Adv. Phys. **64**, 227 (2015).
[6] J. Choi, S. Choi, J. Choi, Y. Park, H. Park, H. Lee, B. Woo, and S. Cho, Phys. Stat. Sol. (b) **241**, 1541 (2004).
[7] J. W. G. Bos, M. Lee, E. Morosan, H. W. Zandbergen, W. L. Lee, N. P. Ong, and R. J. Cava, Phys. Rev. B **74**, 184429 (2006).
[8] Y. S. Hor, P. Roushan, H. Beidenkopf, J. Seo, D. Qu, J. G. Checkelsky, L. A. Wray, D. Hsieh, Y. Xia, S.-Y. Xu, D. Qian, M. Z. Hasan, N. P. Ong, A. Yazdani, and R. J. Cava, Phys. Rev. B **81**, 195203 (2010).
[9] V. Kulbachinskii, A. Kaminskii, K. Kindo, Y. Narumi, K. Suga, P. Lostak, and P. Svanda, Physica B **311**, 292 (2002).
[10] L. J. Collins-McIntyre, L. B. Duffy, A. Singh, N.-J. Steinke, C. J. Kinane, T. R. Charlton, A. Pushp, A. J. Kellock, S. S. P. Parkin, S. N. Holmes, C. H. W. Barnes, G. van der Laan, S. Langridge, and T. Hesjedal, EPL (Europhysics Letters) **115**, 27006 (2016).
[11] A. I. Figueroa, G. van der Laan, L. J. Collins-McIntyre, S.-L. Zhang, A. A. Baker, S. E. Harrison, P. Schönherr, G. Cibin, and T. Hesjedal, Phys. Rev. B **90**, 134402 (2014).
[12] M. Li, C.-Z. Chang, L. Wu, J. Tao, W. Zhao, M. H. W. Chan, J. S. Moodera, J. Li, and Y. Zhu, Phys. Rev. Lett. **114**, 146802 (2015).
[13] C.-Z. Chang, W. Zhao, D. Y. Kim, H. Zhang, B. A. Assaf, D. Heiman, S.-C. Zhang, C. Liu, M. H. W. Chan, and J. S. Moodera, Nat. Mater. **14**, 473 (2015).
[14] L. Zhang, D. Zhao, Y. Zang, Y. Yuan, G. Jiang, M. Liao, D. Zhang, K. He, X. Ma, and Q. Xue, APL Mater. **5**, 076106 (2017).
[15] C.-Z. Chang, J. Zhang, X. Feng, J. Shen, Z. Zhang, M. Guo, K. Li, Y. Ou, P. Wei, L.-L. Wang, Z.-Q. Ji, Y. Feng, S. Ji, X. Chen, J. Jia, X. Dai, Z. Fang, S.-C. Zhang, K. He, Y. Wang, L. Lu, X.-C. Ma, and Q.-K. Xue, Science **340**, 167 (2013).
[16] M. Winnerlein, S. Schreyeck, S. Grauer, S. Rosenberger, K. M. Fijalkowski, C. Gould, K. Brunner, and L. W. Molenkamp, Phys. Rev. Materials **1**, 011201 (2017).
[17] L. B. Duffy, A. I. Figueroa, L. Gładczuk, N.-J. Steinke, K. Kummer, G. van der Laan, and T. Hesjedal, Phys. Rev. B **95**, 224422 (2017).
[18] Y.-J. Chien, *Transition Metal-Doped Sb_2Te_3 and Bi_2Te_3 Diluted Magnetic Semiconductors*, Ph.D. thesis, The University of Michigan (2007).
[19] J. S. Dyck, P. Hájek, P. Lošt'ák, and C. Uher, Phys. Rev. B **65**, 115212 (2002).
[20] P. Larson and W. R. L. Lambrecht, Phys. Rev. B **78**, 195207 (2008).
[21] M. G. Vergniory, M. M. Otrokov, D. Thonig, M. Hoffmann, I. V. Maznichenko, M. Geilhufe, X. Zubizarreta, S. Ostanin, A. Marmodoro, J. Henk, W. Hergert, I. Mertig, E. V. Chulkov, and A. Ernst, Phys. Rev. B **89**, 165202 (2014).
[22] S. Grauer, S. Schreyeck, M. Winnerlein, K. Brunner, C. Gould, and L. W. Molenkamp, Phys. Rev. B **92**, 201304 (2015).
[23] M. Ye, W. Li, S. Zhu, Y. Takeda, Y. Saitoh, J. Wang, H. Pan, M. Nurmamat, K. Sumida, F. Ji, Z. Liu, H. Yang, Z. Liu, D. Shen, A. Kimura, S. Qiao, and X. Xie, Nat. Commun. **6**, 8913 (2015).
[24] P. Sessi, R. R. Biswas, T. Bathon, O. Storz, S. Wilfert, A. Barla, K. A. Kokh, O. E. Tereshchenko, K. Fauth, M. Bode, and A. V. Balatsky, Nat. Commun. **7**, 12027 (2016).
[25] T. R. F. Peixoto, H. Bentmann, S. Schreyeck, M. Winnerlein, C. Seibel, H. Maaß, M. Al-Baidhani, K. Treiber, S. Schatz, S. Grauer, C. Gould, K. Brunner, A. Ernst,

L. W. Molenkamp, and F. Reinert, Phys. Rev. B **94**, 195140 (2016).
[26] B. Leedahl, D. W. Boukhvalov, E. Z. Kurmaev, A. Kukharenko, I. S. Zhidkov, N. V. Gavrilov, S. O. Cholakh, P. H. Le, C. W. Luo, and A. Moewes, Sci. Rep. **7**, 5758 (2017).
[27] W. P. Lin, D. E. Wesolowski, , and C. C. Lee, J. Mater. Sci. Mater. Electron. **22**, 1313 (2011).
[28] M. C. Shaughnessy, J. A. Z. N. C. Bartelt, and J. D. Sugar, J. Appl. Phys. **115**, 063705 (2014).
[29] M. D. Watson, L. J. Collins-McIntyre, L. R. Shelford, A. I. Coldea, D. Prabhakaran, S. C. Speller, T. Mousavi, C. R. M. Grovenor, Z. Salman, S. R. Giblin, G. van der Laan, and T. Hesjedal, New J. Phys. **15**, 103016 (2013).
[30] A. Ghasemi, D. Kepaptsoglou, A. I. Figueroa, G. A. Naydenov, P. J. Hasnip, M. I. J. Probert, Q. Ramasse, G. van der Laan, T. Hesjedal, and V. K. Lazarov, APL Mater. **4**, 126103 (2016).
[31] J. Růžička, O. Caha, V. Holý, H. Steiner, V. Volobuiev, A. Ney, G. Bauer, T. Duchoň, K. Veltruská, I. Khalakhan, V. Matolín, E. F. Schwier, H. Iwasawa, K. Shimada, and G. Springholz, New J. Phys. **17**, 013028 (2015).
[32] A. N. Andriotis and M. Menon, Phys. Rev. B **87**, 155309 (2013).
[33] v. Drašar, J. Kašparová, P. Lošták, X. Shi, and C. Uher, Phys. Stat. Sol. (b) **244**, 2202 (2007).
[34] E. O. Lachman, A. F. Young, A. Richardella, J. Cuppens, H. R. Naren, Y. Anahory, A. Y. Meltzer, A. Kandala, S. Kempinger, Y. Myasoedov, M. E. Huber, N. Samarth, and E. Zeldov, Sci. Adv. **1**, e1500740 (2015).
[35] G. van der Laan and A. I. Figueroa, Coord. Chem. Rev. **277–278**, 95 (2014).
[36] A. I. Figueroa, G. van der Laan, S. E. Harrison, G. Cibin, and T. Hesjedal, Sci. Rep. **6**, 22935 (2016).
[37] I. Vobornik, U. Manju, J. Fujii, F. Borgatti, P. Torelli, D. Krizmancic, Y. S. Hor, R. J. Cava, and G. Panaccione, Nano Lett. **11**, 4079 (2011).
[38] S.-Y. Xu, M. Neupane, C. Liu, D. Zhang, A. Richardella, L. A. Wray, N. Alidoust, M. Leandersson, T. Balasubramanian, J. Sanchez-Barriga, O. Rader, G. Landolt, B. Slomski, J. H. Dil, J. Osterwalder, T.-R. Chang, H.-T. Jeng, H. Lin, A. Bansil, N. Samarth, and M. Z. Hasan, Nature Phys. **8**, 616 (2012).
[39] I. Vobornik, G. Panaccione, J. Fujii, Z.-H. Zhu, F. Offi, B. R. Salles, F. Borgatti, P. Torelli, J. P. Rueff, D. Ceolin, A. Artioli, M. Unnikrishnan, G. Levy, M. Marangolo, M. Eddrief, D. Krizmancic, H. Ji, A. Damascelli, G. van der Laan, R. G. Egdell, and R. J. Cava, J. Phys. Chem. C **118**, 12333 (2014).
[40] L. J. Collins-McIntyre, M. D. Watson, A. A. Baker, S. L. Zhang, A. I. Coldea, S. E. Harrison, A. Pushp, A. J. Kellock, S. S. P. Parkin, G. van der Laan, and T. Hesjedal, AIP Adv. **4**, 127136 (2014).
[41] B. Deng, Y. Zhang, S. B. Zhang, Y. Wang, K. He, and J. Zhu, Phys. Rev. B **94**, 054113 (2016).
[42] S. E. Harrison, S. Li, Y. Huo, B. Zhou, Y. L. Chen, and J. S. Harris, Appl. Phys. Lett. **102**, 171906 (2013).
[43] B. Ravel and M. Newville, J. Synchrotron Rad. **12**, 537 (2005).
[44] B. Ravel, J. Synchrotron Rad. **8**, 314 (2001).
[45] K. Fabian, V. P. Shcherbakov, and S. A. McEnroe, Geochem. Geophys. Geosys. **14**, 947 (2013).
[46] A. Roy, S. Guchhait, R. Dey, T. Pramanik, C.-C. Hsieh, A. Rai, and S. K. Banerjee, ACS Nano **9**, 3772 (2015).
[47] S. J. Youn, S. K. Kwon, and B. I. Min, J. Appl. Phys. **101**, 09G522 (2007).
[48] T. Hamasaki, T. Hashimoto, Y. Yamaguchi, and H. Watanabe, Solid State Commun. **16**, 895 (1975).
[49] M. Ye, W. Li, S. Zhu, Y. Takeda, Y. Saitoh, J. Wang, H. Pan, M. Nurmamat, K. Sumida, F. Ji, Z. Liu, H. Yang, Z. Liu, D. Shen, A. Kimura, S. Qiao, and X. Xie, Nat. Commun. (2015).
[50] H. Ofuchi, N. Ozaki, N. Nishizawa, H. Kinjyo, S. Kuroda, and K. Takita, AIP Conf. Proc. **882**, 517 (2007).
[51] B. T. Thole, G. van der Laan, J. C. Fuggle, G. A. Sawatzky, R. C. Karnatak, and J. M. Esteva, Phys. Rev. B **32**, 5107 (1985).
[52] G. van der Laan, Lect. Notes Phys. **697**, 143 (2006).
[53] R. D. Cowan, *The Theory of Atomic Structure and Spectra* (University of California Press, Berkeley, 1981).
[54] G. van der Laan and B. T. Thole, Phys. Rev. B **43**, 13401 (1991).
[55] K. Yaji, A. Kimura, M. Koyama, C. Hirai, H. Sato, K. Shimada, A. Tanaka, and M. Taniguchi, J. Appl. Phys. **97**, 10A316 (2005).
[56] A. A. Baker, A. I. Figueroa, K. Kummer, L. J. Collins-McIntyre, T. Hesjedal, and G. van der Laan, Phys. Rev. B **92**, 094420 (2015).
[57] Z. Zhou, Y.-J. Chien, and C. Uher, Phys. Rev. B **74**, 224418 (2006).
[58] J. Dijkstra, H. H. Weitering, C. F. van Bruggen, C. Haas, and R. A. de Groot, J. Phys.: Cond. Matter **1**, 9141 (1989).
[59] T. Hashimoto, K. Hoya, M. Yamaguchi, and I. Ichitsubo, J. Phy. Soc. Jpn. **31**, 679 (1971).
[60] H. Tan, J. Verbeeck, A. Abakumov, and G. Van Tendeloo, Ultramicroscopy **116**, 24 (2012).
[61] D. Maganas, M. Roemelt, T. Weyhermüller, R. Blume, M. Hävecker, A. Knop-Gericke, S. DeBeer, R. Schlögl, and F. Neese, Phys. Chem. Chem. Phys. **16**, 264 (2014).
[62] B. Jeon, C. Ko, A. C. T. van Duin, and S. Ramanathan, Surf. Sci. **606**, 516 (2012).
[63] G. van der Laan and I. W. Kirkman, J. Phys.: Condens. Matter **4**, 4189 (1992).
[64] M. Copel, M. C. Reuter, E. Kaxiras, and R. M. Tromp, Phys. Rev. Lett. **63**, 632 (1989).
[65] J. Massies and N. Grandjean, Phys. Rev. B **48**, 8502 (1993).
[66] E. Tournié, N. Grandjean, A. Trampert, J. Massies, and K. Ploog, J. Cryst. Growth **150**, 460 (1995).
[67] E. Tournié and K. H. Ploog, Thin Solid Films **231**, 43 (1993).